Spectral indices, particle ages, and the ambient medium of giant radio galaxies

K.-H. Mack[1,2]**, U. Klein**[1]**, C.P. O'Dea**[3]**, A.G. Willis**[4]**, and L. Saripalli**[1,5]

[1]Radioastronomisches Institut, Universität Bonn, Auf dem Hügel 71, D-53121 Bonn, Germany
[2]Istituto di Radioastronomia del CNR, Via P. Gobetti 101, I-40129 Bologna, Italy
[3]Space Telescope Science Institute, 3700 San Martin Drive, Baltimore, MD 21218, USA
[4]Dominion Radio Astrophysical Observatory, P. O. Box 248, Penticton, BC, V2A 6K3, Canada
[5]Raman Research Institute, Sadashiva Nagar, Bangalore 560 080, India

Abstract. We present a spectral aging study of a sample of 5 giant radio galaxies based on radio continuum data obtained at frequencies between 326 MHz and 10.6 GHz. Using synchrotron loss models, we determined injection spectral indices and particle ages where possible. The results suggest ages not older than $4 \cdot 10^7$ yr, a value that is typical for radio galaxies with "normal" sizes. From equilibrium considerations between lobes and jets on the one hand and the ambient medium on the other we derived estimates of the density of the intergalactic medium, with average values in the range of a few 10^{-5} cm^{-3}.

Key words: radio continuum: galaxies – galaxies: individual: NGC 315; DA 240; 3C 236; 3C 326; NGC 6251

1. Introduction

Giant radio galaxies (GRGs) form a somewhat special class of extragalactic radio sources. Their linear projected sizes of ≥ 1 Mpc, which is the criterion of their membership to this class, immediately prompts the question of their likely special nature. The total luminosity of GRGs ranks them in the transition regime between FR-I (low-power systems) and FR-II (high-power ones), so they are neither extremely powerful nor particularly weak. One possibility is that very powerful active galactic nuclei (AGN) could drive them to their extraordinary sizes. On the other hand, sources that have expanded to such sizes could also have undergone strong adiabatic losses, resulting in low or moderate total luminosities. In fact, in order to explain the observed relative numbers of radio sources as a function of linear size, their radio power must drop as the inverse square root of linear size (O'Dea & Baum 1997). Therefore, this picture is not quite clear. An alternative conjecture is that the extreme sizes

Send offprint requests to: K.-H. Mack, Bologna address

of GRGs are simply related to their surrounding intergalactic medium (IGM), which is difficult to access directly via observations. It is one of the prime aims of this paper to explore this latter hypothesis.

There are several tools to probe the IGM density. Firstly, we can simply balance pressures; the pressure of the relativistic particles and magnetic fields of the radio source must be of the same order of magnitude as the external thermal pressure. In order to get a handle on this internal pressure, the intensity distribution across the radio source must be mapped over a frequency range as large as possible. The second tool comes via radio polarization, viz. Faraday rotation. The latter is very sensitive to the density, or variations in the density, of the thermal plasma mixed with the source or surrounding it. Thirdly, the impinging jet experiences ram pressure by the external medium. In this paper we shall try to derive a consistent picture on the likely state of the environment of GRGs and thus contribute to an understanding of their nature.

Spectral index investigations of radio galaxies have frequently been carried out in the past. They were performed for various types of sources with different frequency pairs. Most of these studies used frequencies in the range between 0.6 and 1.4 GHz; they indicated trends in the spectral index distribution which should be much more obvious when we use a broader frequency range. While the sources are in principle "in their original state" at low frequencies, without having suffered from severe synchrotron losses, at high frequencies aging effects should be more apparent and we expect to see only the brightest or most active regions of the sources in high-frequency images. In this paper we use the data shown in Mack et al. (1997) to derive the spectral characteristics of five of the most extended GRGs in the frequency range between 326 MHz and 10.6 GHz (Sect. 2). We will present similar analyses for less extended radio galaxies using 10.6-GHz and lower-frequency maps in another paper. Using the spectral information we determine relevant physical parameters of the sources and their components. Energies and
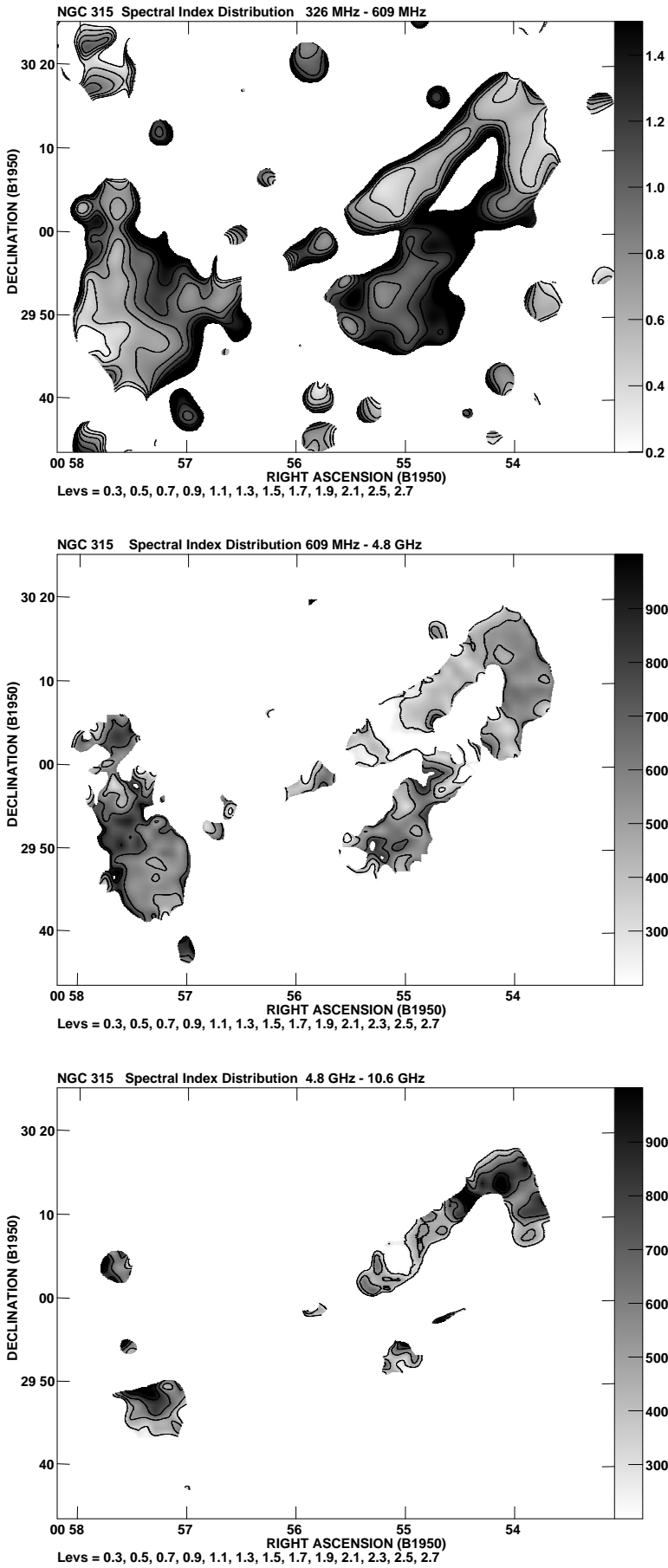
Fig. 1. Spectral index maps of NGC 315.

Table 1. Physical parameters of NGC 315

Region	Volume [cm^3]	α_{326}^{10550}	Total luminosity [erg sec^{-1}]	U_{eq} [erg]	u_{eq} [erg cm^{-3}]	H_{eq} [μG]	α_{inj}	t [Myr]
total	$2.98 \cdot 10^{72}$	0.43	$7.7 \cdot 10^{41}$	$4.6 \cdot 10^{58}$	$1.6 \cdot 10^{-14}$	0.5	–	–
1	$7.22 \cdot 10^{70}$	0.29	$5.0 \cdot 10^{41}$	$6.2 \cdot 10^{57}$	$8.6 \cdot 10^{-13}$	1.2	–	–
2	$1.74 \cdot 10^{70}$	0.60	$9.8 \cdot 10^{39}$	$5.5 \cdot 10^{56}$	$3.2 \cdot 10^{-14}$	0.7	0.59	≤ 12.0
3	$5.72 \cdot 10^{70}$	0.50	$6.1 \cdot 10^{40}$	$2.3 \cdot 10^{57}$	$3.9 \cdot 10^{-14}$	0.8	0.54	≤ 12.0
4	$4.72 \cdot 10^{70}$	0.53	$3.8 \cdot 10^{40}$	$1.6 \cdot 10^{57}$	$3.5 \cdot 10^{-14}$	0.7	0.56	≤ 12.5
5	$1.06 \cdot 10^{71}$	0.27	$4.7 \cdot 10^{40}$	$1.9 \cdot 10^{57}$	$1.7 \cdot 10^{-14}$	0.5	–	–
6	$1.10 \cdot 10^{72}$	0.72	$3.7 \cdot 10^{40}$	$8.7 \cdot 10^{57}$	$7.9 \cdot 10^{-15}$	0.4	0.58	≤ 8.5
7	–	–	–	–	–	–	–	–
9	$4.00 \cdot 10^{71}$	0.55	$6.8 \cdot 10^{40}$	$5.9 \cdot 10^{57}$	$1.5 \cdot 10^{-14}$	0.5	0.58	≤ 9.4
10	$1.18 \cdot 10^{72}$	0.82	$2.2 \cdot 10^{40}$	$8.0 \cdot 10^{57}$	$6.8 \cdot 10^{-15}$	0.3	–	–

magnetic fields are necessary ingredients to a particle aging analysis. There have been many studies applying synchrotron loss models to the determination of particle ages (e.g. van der Laan & Perola 1969; Pacholczyk 1970; Myers & Spangler 1985; Alexander & Leahy 1987; Carilli et al. 1991). In addition to these more "classical" methods, Katz-Stone (1995) and Rudnick & Katz-Stone (1996) discussed a number of new tools for the analysis of synchrotron source maps. These authors pointed out that the traditional methods might miss information. Nevertheless, to start with, we follow the classical spectral analysis methods.

The different tools to probe the characteristics of the IGM with the help of GRGs have been summarized by Saripalli (1988). Besides various statistical tests, such as clustering of galaxies around the radio source, the effects of the external gas on the radio jets and lobes appear to be important (Subrahmanyan & Saripalli 1993; Lacy et al. 1993; Daly 1995; Nath 1995). In Sects. 3 and 4 we present our investigation of the density of the IGM around the most extended GRGs, which has been based on equilibrium considerations between the radio lobes and the IGM. Throughout this analysis we adopt $H_0 = 75$ km s^{-1} Mpc^{-1} and $q_0 = 1$.

2. Spectral indices

We have made maps of the spectral index α ($I_\nu \propto \nu^{-\alpha}$) for all sources. To this end, we have smoothed the higher-resolution maps to a common beam size of $150''$ via an image plane convolution. The spectral index was calculated only within regions with intensities higher than 2σ. We have made sure that systematic errors as listed by Strom et al. (1981) can be neglected in most areas of the maps. All data have been carefully checked concerning calibration scales or zero levels. Coordinate errors are expected to be clearly below $5''$. Projection errors do not occur because all data have been interpolated onto the same projection grid. Errors due to beamshape differences are only important at λ6-cm in the surroundings of very bright peaks like the core of 3C 236, or the hot spot of DA 240. Because of the much more complex beam CLEANing, the removal of dirty beam residuals at λ 6 cm did not work as properly as in the case of the λ2.8-cm maps (Mack et al. 1997). We present three

maps for each source displaying the low-frequency (α_{325}^{609}), the intermediate-frequency (α_{609}^{4750}), and the high-frequency (α_{4750}^{10550}) spectral index distribution.

2.1. NGC 315

Spectral index studies of this source have been performed by Willis et al. (1981) who showed crosscuts of the spectral index along the jet and counter jet and also presented the spectral index distribution of the north-west lobe. Already noted also by other authors (Fanti et al. 1976, Bridle & Fomalont 1978) was the much flatter spectrum along the main and counter jet. Willis et al. (1981) found significant spectral variation over the north-western lobe, with a steepening from the northern edge to the southern parts. The south-eastern lobe, however, was found to have a very constant spectral index. Using the upgraded WSRT, Jägers (1987) basically confirmed the global spectral behaviour described by Willis et al. (1981). Because of the better resolution, however, he also detected small-scale areas with steep spectra, coincident with peaks in the total intensity distribution.

In Fig. 1 we show our spectral index maps of NGC 315. The core shows a flat spectrum with a further flattening toward high frequencies. The north-western jet has an almost constant spectral index at low- and intermediate frequencies, with a steeper-spectrum zone shortly before the hotspot is reached. This is especially striking at high frequencies. The counter jet, which is seen only over a short distance, appears to have a slightly steeper spectrum until it is below the sensitivity of the maps. Although the beam sizes have been checked carefully we are not sure about the reliability of the steep-spectrum limbs especially of the jets. The north-western hot spot area steepens gradually from the north-east to the south-west. The bright lobe is somewhat steeper at high frequencies, with a more or less constant spectrum. The back-lobe spectrum is generally steep ($\alpha \approx 1.3$) with flat-spectrum islands ($\alpha = 0.62 \pm 0.14$) in between, especially in the south-eastern parts. The south-western lobe shows a region with a spectrum which is flat compared with its environment. This region could mark the channel where the counter jet runs through the lobe. The eastern lobe spectrum is steeper than the western one except for the back-lobe.
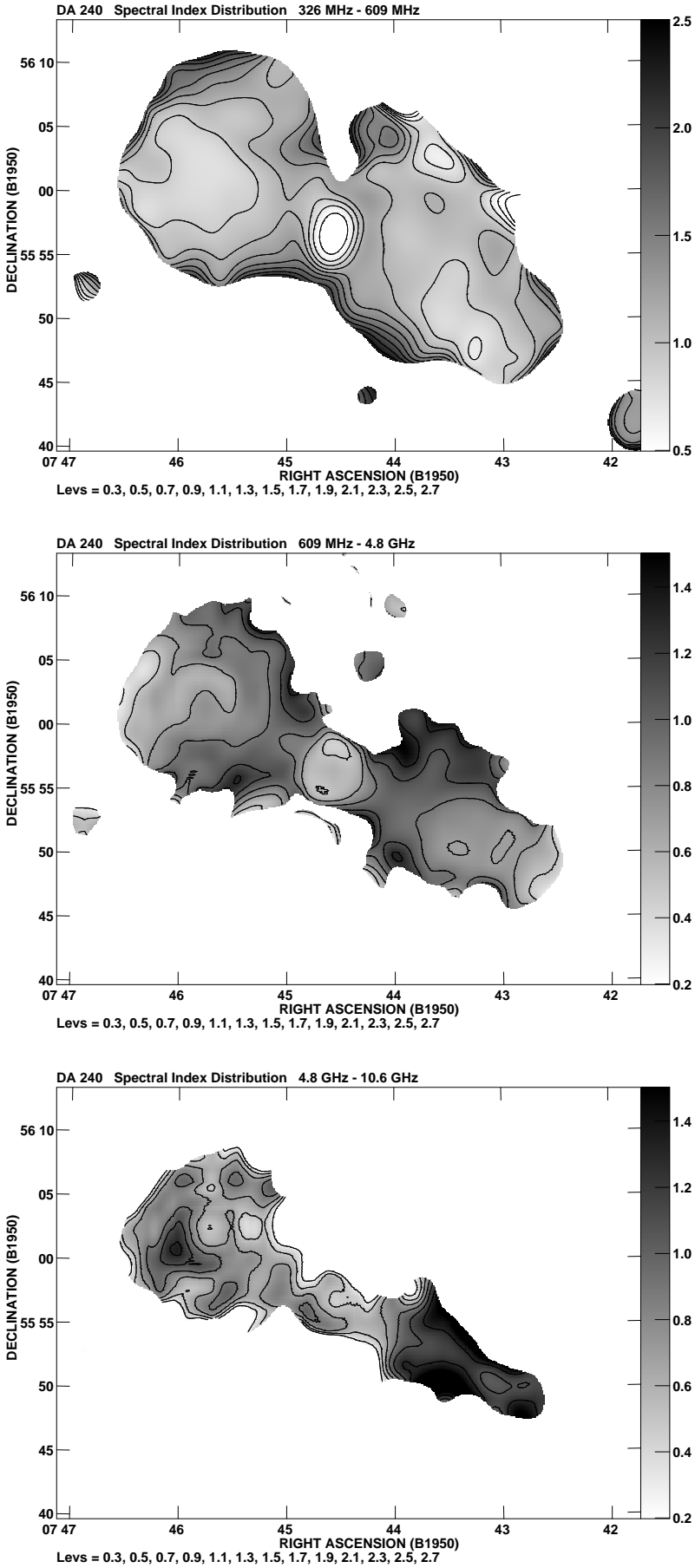
Fig. 2. Spectral index maps of DA 240.

Table 2. Physical parameters of DA 240

Region	Volume [cm^3]	α_{326}^{10550}	Total luminosity [erg sec^{-1}]	U$_{eq}$ [erg]	u$_{eq}$ [erg cm^{-3}]	H$_{eq}$ [μG]	α_{inj}	t [Myr]
total	$1.65 \cdot 10^{73}$	0.80	$1.8 \cdot 10^{42}$	$2.9 \cdot 10^{59}$	$1.8 \cdot 10^{-14}$	0.5	–	–
1	$9.55 \cdot 10^{72}$	0.75	$1.2 \cdot 10^{42}$	$1.7 \cdot 10^{59}$	$1.8 \cdot 10^{-14}$	0.5	0.76	≤ 9.4
2	$6.93 \cdot 10^{72}$	0.99	$4.5 \cdot 10^{41}$	$1.3 \cdot 10^{59}$	$1.9 \cdot 10^{-14}$	0.5	0.97	≤ 10.6
3	–	0.56	$1.2 \cdot 10^{42}$	–	–	–	–	–

2.2. DA 240

Strom et al. (1981) published a spectral index map of DA 240 based on observations at $\lambda\lambda$ 49 cm and 6 cm. They found a narrow, relatively flat-spectrum region along the source major axis which connects the core and the outer hot spots. Flatter spectra were also detected in the regions near the leading edge of both components, and along the southern rim of the eastern lobe, although the global behaviour that Strom et al. (1981) reported is a significant steepening from the centre to the outer limb of both components. The flatter spectrum bridge connecting the core and the outer lobe areas along the source's main axis is also the most striking feature in our spectral index distribution maps (Fig. 2). The core and the bright eastern hot spot still suffer from artifacts of insufficient CLEANing where the 4.8-GHz map is involved. In all three maps the regions around the flat-spectrum core are amongst those with the steepest spectra. Toward the outer regions of DA 240, the spectrum gradually flattens along the major axis, while it steepens perpendicular to it. At high frequencies there appears to be an asymmetry between the lobes, with a difference of $\Delta\alpha \approx 0.4$ between the flatter western and the steeper eastern lobe.

2.3. 3C 236

The first spectral index study of 3C 236 was performed by Strom & Willis (1980). They used maps obtained at 609 MHz, 1.4, and 5 GHz with the WSRT. Although the higher-frequency maps were affected by missing-spacing effects these authors found a significant steepening of the spectrum in the north-western lobe toward the core and an indication for a flattening of the spectrum of the outer head between 1.4 and 5 GHz compared with the 609 – 1400 MHz spectral index. Strom et al. (1981) presented a spectral index map derived from a 609-MHz WSRT map and a 4.8-GHz Effelsberg map and confirmed these results.

　　In our spectral index maps (Fig. 3) the north-western lobe clearly shows gradual steepening from the hot spot at the lobe's edge toward the core. The south-eastern lobe spectrum is complex, mainly because of confusion by the flat background source north of the major axis and the steep-spectrum background source at the southern termination of this lobe. Nevertheless, the steepening of the spectrum toward the core is also visible even at higher frequencies. There is a tendency for the spectrum in the north-western lobe to be generally steeper than that of the south-eastern one. The asymmetry becomes more obvious looking at the high-frequency spectral index map. The core is

surrounded by artificial structures which are due to insufficient CLEANing of the 6-cm single-horn data (Mack et al. 1997).

2.4. 3C 326

Willis & Strom (1978) showed crosscuts of the spectral index distribution along the source's major axis, derived from measurements at 609 MHz and 1.4 GHz. They did not find any significant spatial variation in the spectral index over the eastern lobe or variations of the spectrum itself. In the western lobe they observed a gradual steepening from the lobe's termination toward the core without any distinct peaks.

　　This gradual steepening can also be found in our high-frequency spectral index map (Fig. 4). The low-frequency spectral index map does not show much variable structure, either in the eastern or in the central and western components. At high frequencies a flatter-spectrum channel is indicated crossing the eastern lobe, similar to the situation in the south-eastern lobe of NGC 315. The background source to the west of 3C 326 has a significantly steeper spectrum than the feature at the termination of the western lobe.

2.5. NGC 6251

Waggett et al. (1977) presented the first spectral index map of this source from observations between 151 and 1417 MHz. They found a mean spectral index of the jet of $\alpha = 0.54$ and steeper spectra in the outer parts of the source ($\alpha \in [0.5, 1.0]$), with extreme values $\alpha > 1.3$ in the outermost western part of the source. The spectral behaviour of the famous jet of NGC 6251 has been investigated by Saunders et al (1981) and by Perley et al. (1984) in great detail.

　　In Fig. 5 we present the spectral index distribution of NGC 6251. The low-frequency spectral index map displays steep-spectrum regions in the outer lobes ($\alpha \approx 1.7$) which are below the range of significance at higher frequencies. Significant spectral asymmetries are not present at these low frequencies. The core has a flat spectrum. The jet spectrum is very typical ($\alpha = 0.6$), with a gradual steepening to 0.8 shortly before it widens up and mixes with the diffuse lobe emission. The steep spectrum of the counter-jet feature does not support the relationship of this region to an actual counter jet as has been inferred from morphological arguments. The hot spot spectra are very different at high frequencies. While the north-western one possesses a high-frequency spectral index of $\alpha = 0.79 \pm 0.01$, the south-eastern one is significantly steeper ($\alpha = 1.2 \pm 0.04$).
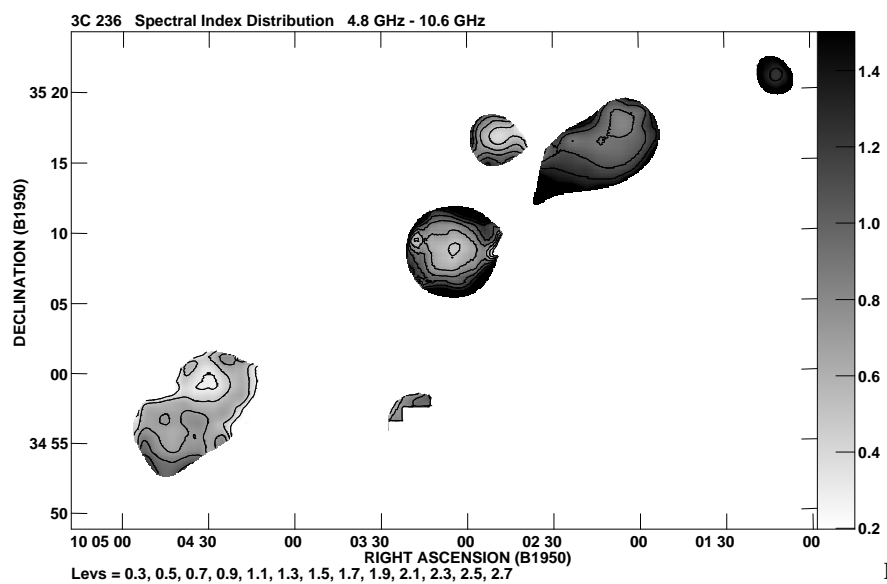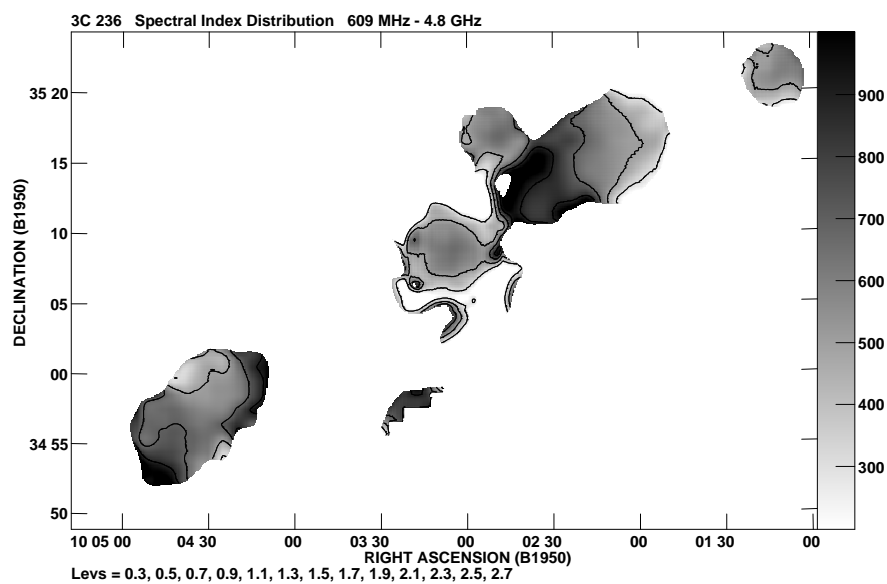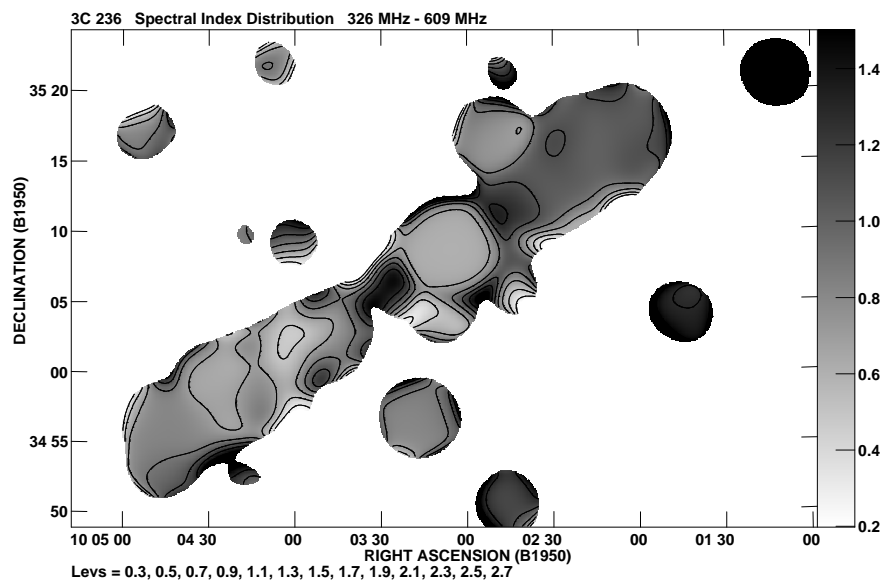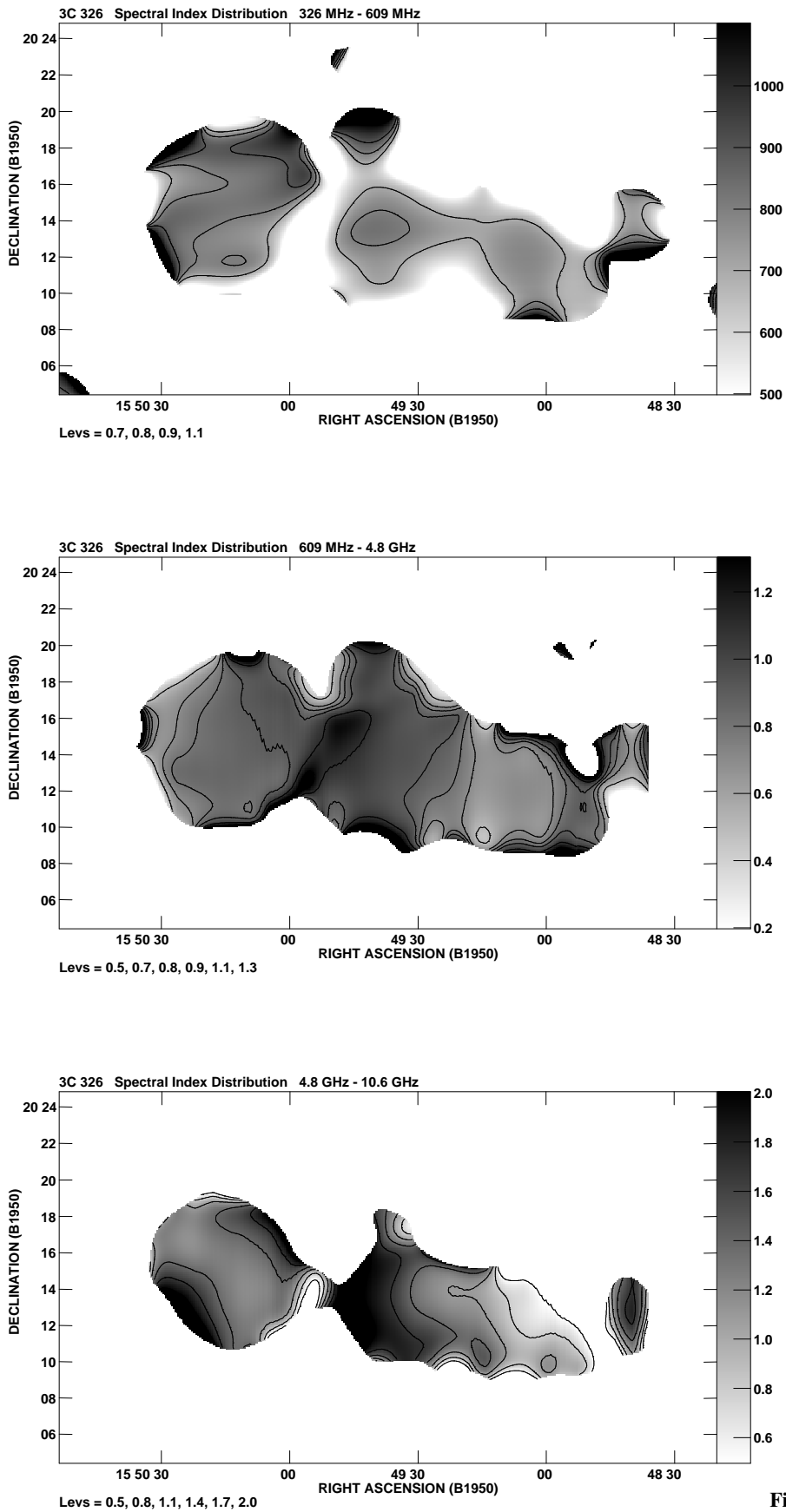
Fig. 3. Spectral index maps of 3C 236

3C 326   Spectral Index Distribution   326 MHz - 609 MHz

Levs = 0.7, 0.8, 0.9, 1.1

3C 326   Spectral Index Distribution   609 MHz - 4.8 GHz

Levs = 0.5, 0.7, 0.8, 0.9, 1.1, 1.3

3C 326   Spectral Index Distribution   4.8 GHz - 10.6 GHz

Levs = 0.5, 0.8, 1.1, 1.4, 1.7, 2.0

Fig. 4. Spectral index maps of 3C 326

Table 3. Physical parameters of 3C 236

Region	Volume [cm^3]	α_{326}^{10550}	Total luminosity [erg sec^{-1}]	U_{eq} [erg]	u_{eq} [erg cm^{-3}]	H_{eq} [μG]	α_{inj}	t [Myr]
total	$2.87 \cdot 10^{73}$	0.67	$1.53 \cdot 10^{43}$	$1.0 \cdot 10^{60}$	$3.5 \cdot 10^{-14}$	0.7	–	–
1	–	0.61	$1.05 \cdot 10^{43}$	–	–	–	–	–
2	$1.29 \cdot 10^{73}$	0.77	$5.11 \cdot 10^{41}$	$1.2 \cdot 10^{59}$	$9.5 \cdot 10^{-15}$	0.4	0.70	≤ 7.3
3	$5.69 \cdot 10^{72}$	0.69	$1.39 \cdot 10^{42}$	$1.3 \cdot 10^{59}$	$2.3 \cdot 10^{-14}$	0.6	0.70	≤ 7.8
4	$7.60 \cdot 10^{72}$	0.93	$1.18 \cdot 10^{42}$	$2.1 \cdot 10^{59}$	$2.8 \cdot 10^{-14}$	0.7	0.73	7.2
6	$2.53 \cdot 10^{72}$	0.76	$9.49 \cdot 10^{41}$	$8.5 \cdot 10^{58}$	$3.4 \cdot 10^{-14}$	0.7	0.50	20.3

Table 4. Physical parameters of 3C 326

Region	Volume [cm^3]	α_{326}^{10550}	Total luminosity [erg sec^{-1}]	U_{eq} [erg]	u_{eq} [erg cm^{-3}]	H_{eq} [μG]	α_{inj}	t [Myr]
total	$7.80 \cdot 10^{72}$	0.95	$5.87 \cdot 10^{42}$	$5.5 \cdot 10^{59}$	$7.0 \cdot 10^{-14}$	1.1	–	–
1	$4.54 \cdot 10^{72}$	0.97	$3.25 \cdot 10^{42}$	$3.2 \cdot 10^{59}$	$7.1 \cdot 10^{-14}$	1.1	0.61	27.0
2	$1.73 \cdot 10^{72}$	1.05	$1.47 \cdot 10^{42}$	$1.5 \cdot 10^{59}$	$8.9 \cdot 10^{-14}$	2.4	0.58	18.5
3	$1.53 \cdot 10^{72}$	0.75	$1.16 \cdot 10^{42}$	$2.0 \cdot 10^{59}$	$1.3 \cdot 10^{-14}$	0.5	0.62	10.3

3. Energies, magnetic fields, and particle aging

Because of the complex morphologies of the sources we have estimated the volumes by adding up their individual components corresponding to the regions defined in Mack et al. (1997). For the sake of clarity we show these regions in the "finding charts"(Fig. 6). The source diameters have mainly been determined from the radio maps at the highest angular resolution (i.e. at 609 MHz) unless missing spacings obviously affect the results. In these cases we used the 326-MHz map. The volumes are based on cylinder geometry, with effective deconvolved angular sizes derived as described by Burns et al. (1979).

Knowing the volumes V and radio luminosities L we have calculated magnetic field strengths H_{eq} and particle energies U_{eq} based on equipartition assumptions. This has been done following the formulae given by Pacholczyk (1970):

$$H_{eq} = \left(\frac{V\Phi}{6\pi (1 + k) c_{12}L} \right)^{-\frac{2}{7}}$$

$$U_{eq} = \frac{7}{4} ((1 + k) c_{12}L)^{\frac{4}{7}} \left(\frac{\Phi V}{6\pi} \right)^{\frac{3}{7}}$$

Both the filling factor Φ and the proton-electron energy ratio k have been assumed to be unity. c_{12} is a constant as given by Pacholzcyk (1970), that is mainly dependent on the spectral index. The spectral index used was that determined from our maps between 326 MHz and 10.6 GHz. The results of these calculations are shown for each source and its components in Tables 1 – 5.

Kardashev (1962) studied the basic synchrotron loss models which were later used by other authors to derive actual source ages. Van der Laan & Perola (1969), Roland et al. (1985, 1990) and Roland & Rhee (1989) discussed the importance of diffusion in the loss scenarios. Presently it is assumed that diffusion

losses are small compared to radiative losses. Neglecting these we have tried to fit different synchrotron models to the radio data using the code described by Carilli et al. (1991). In particular these models are:

- the continuous injection (CI) model which assumes a mixture of electron populations of various synchrotron ages. In this model there is permanent replenishment of fresh particles so that the injection spectral index α_{inj} steepens only by $\alpha_{inj} + 0.5$ beyond the break frequency.
- the Kardashev-Pacholczyk (KP) model which merely includes a single injection of power-law distributed electrons (Kardashev 1962, Pacholczyk 1970). The pitch angles of the electrons are assumed to be constant with time. The high-frequency slope in this model is $\frac{4}{3}\alpha_{inj} + 1$.
- the Jaffe-Perola (JP) model (Jaffe & Perola 1973) which – similar to KP – incorporates a single injection but permits permanent pitch angle isotropization. Beyond the spectral break frequency this model leads to an exponential steepening of the high-frequency spectrum.

By running the fit routine several times we have tried to get the best α_{inj}. As a criterion for the quality of the fit we took reduced χ^2 values which are provided by the programme. From the break frequencies we have calculated particle ages according to Alexander & Leahy (1987):

$$t = 1.59 \cdot 10^3 \frac{\sqrt{H_{eq}}}{H_{eq}^2 + H_{IC}^2} \frac{1}{\sqrt{\nu_B(1 + z)}}$$

Here, t is the particle age in Myr, $H_{IC} = 3.25(1 + z)^2$ is the magnetic field equivalent to the microwave background in μG, ν_B is the break frequency in GHz. We have excluded the cores, where we do not expect to see synchrotron losses, and background sources which do not belong to the radio galaxies. There are some cases where the fits yield break frequencies more than
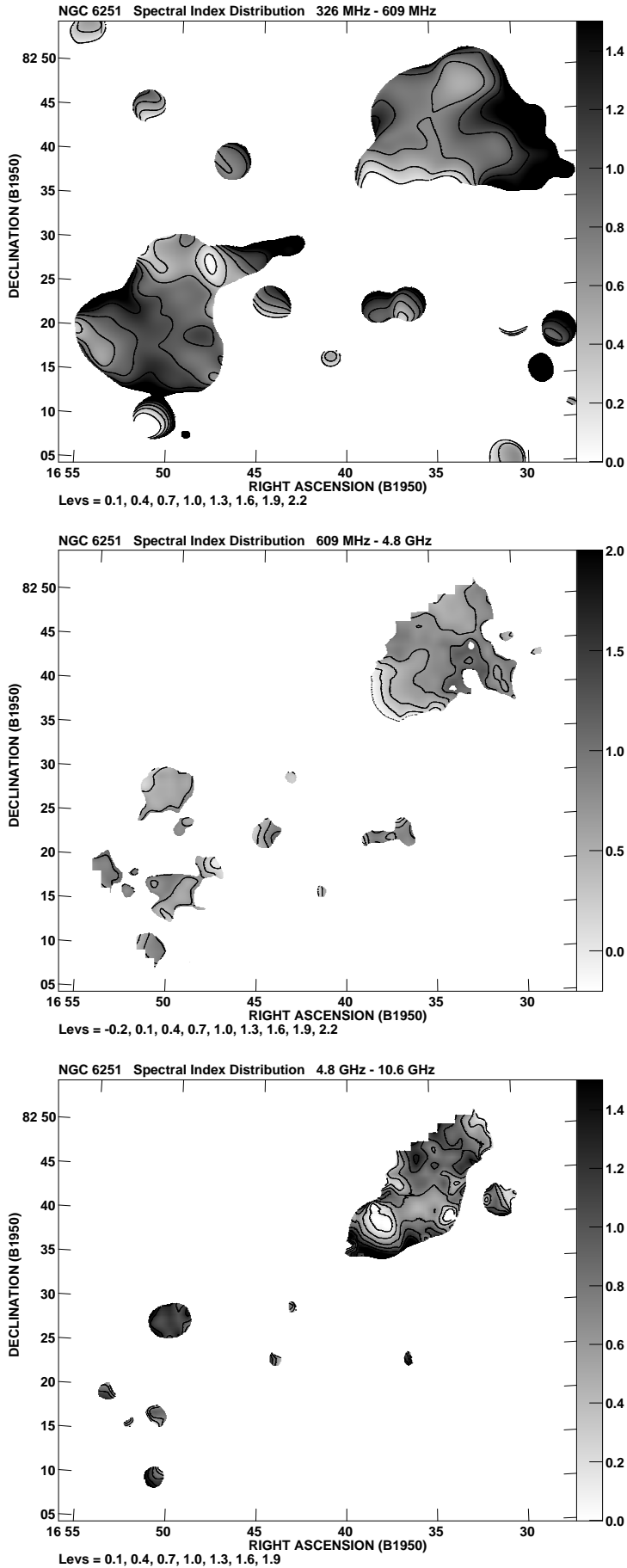
Fig. 5. Spectral index maps of NGC 6251

Table 5. Physical parameters of NGC 6251

Region	Volume [cm^3]	α_{326}^{10550}	Total luminosity [erg sec^{-1}]	U_{eq} [erg]	u_{eq} [erg cm^{-3}]	H_{eq} [μG]	α_{inj}	t [Myr]
total	$2.26 \cdot 10^{73}$	0.58	$1.0 \cdot 10^{42}$	$1.6 \cdot 10^{59}$	$7.2 \cdot 10^{-15}$	0.3	–	–
1	$1.82 \cdot 10^{71}$	0.40	$8.3 \cdot 10^{41}$	$1.4 \cdot 10^{58}$	$7.7 \cdot 10^{-14}$	1.1	–	–
2	$1.06 \cdot 10^{73}$	0.77	$1.5 \cdot 10^{41}$	$5.6 \cdot 10^{58}$	$5.3 \cdot 10^{-15}$	0.3	0.78	≤ 42
3	$6.62 \cdot 10^{72}$	0.60	$4.7 \cdot 10^{40}$	$1.7 \cdot 10^{58}$	$2.6 \cdot 10^{-15}$	0.2	0.56	7.6
6	$2.11 \cdot 10^{70}$	0.55	$3.2 \cdot 10^{40}$	$1.1 \cdot 10^{57}$	$5.1 \cdot 10^{-14}$	0.9	0.60	≤ 12
7	$4.15 \cdot 10^{70}$	1.41	$7.0 \cdot 10^{39}$	$2.1 \cdot 10^{57}$	$5.0 \cdot 10^{-14}$	0.9	0.53	≤ 13
8	$5.14 \cdot 10^{72}$	1.62	$1.1 \cdot 10^{41}$	$9.0 \cdot 10^{58}$	$1.8 \cdot 10^{-14}$	0.5	0.67	41

an order of magnitude greater than the highest observation frequency, i.e. higher than 105 GHz. In these cases we took 105 GHz as a lower limit to the break frequency and calculated upper limits to the particle ages. For the cases where a fit was possible we have listed α_{inj} and t in Table 1 – 5. In all cases the JP spectrum yielded lower or similar χ^2 values compared to the KP model. In the latter cases we preferred the JP model which may be the more physical scenario as it allows for pitch angle isotropization.

4. The ambient medium

Since the GRGs probe the density of the IGM we have used the parameters derived above to determine particle densities of the ambient medium. We have balanced the pressure exerted by the relativistic gas in the radio lobes ($\frac{1}{3}u_{eq}$, u_{eq} given in Tables 1 – 5) against the pressure of the IGM ($n_{eq}kT$). This leads to the particle density via

$$n_{eq}[cm^{-3}] = \frac{u_{eq}}{3k\,T}$$

Here k is the Boltzmann constant and T the temperature of the IGM (in K). We have assumed temperatures of 10^7 K. The resulting densities are compiled in Table 6.

A second method to determine densities of the ambient medium is the depolarization analysis. In a preliminary study of the polarization data of these sources Klein et al. (1996) found average densities of a few 10^{-5} cm^{-3}.

For comparison, we have balanced in a way similar to the calculations of Lacy et al. (1993) the momentum flux of the jet against the ram pressure of the external medium over an impact area A. The head of the source is assumed to advance at speed β (in units of c^{-1}, c = velocity of light). This yields an estimate of the density of the IGM via

$$n_{rp}[cm^{-3}] = 5.32 \cdot 10^{-6} \left(\frac{U_{eq}}{10^{-59}\text{erg}}\right) \left(\frac{t}{\text{Myr}}\right)^{-1} \beta^{-2} \left(\frac{A}{\text{kpc}^2}\right)^{-1}$$

For the constant term a mean atomic weight of 1.4 amu has been assumed. If U_{eq} is taken as the total energy of the source it should be divided by a factor of 2 since the energy is conveyed in two jets.

The lobe advance speed has often been determined from spectral aging investigations. This can, however, lead to an

Table 6. Impact areas and particle densities

Source	n_{eq} [cm^{-3}]	impact area [kpc^2]	n_{rp} [cm^{-3}]
NGC 315	$3.0 \cdot 10^{-5}$	59	$\geq 3.8 \cdot 10^{-6}$
DA 240	$9.2 \cdot 10^{-6}$	79	$\geq 1.0 \cdot 10^{-5}$
3C 236	$1.5 \cdot 10^{-5}$	38	$3.8 \cdot 10^{-5}$
3C 326	$3.3 \cdot 10^{-5}$	59	$1.0 \cdot 10^{-5}$
NGC 6251	$1.8 \cdot 10^{-5}$	59	$2.0 \cdot 10^{-6}$

overestimate of the speed when particle back-flow and advance speeds are superposed (Scheuer 1995). Therefore, we took an average value of 0.03c which is consistent with the results found by other authors (Lacy et al. 1993), and complies with the findings of Scheuer (1995) who concludes that the growth speeds of lobes are typically a few per cent of the speed of light.

The effective area A of the drilling jet is also difficult to determine. We refer to higher-frequency data reported in the literature. Realistic estimates for the effective areas are only available for two of the sources, DA 240 and 3C 236. Tsien (1992) presented a detailed study of the eastern hot spot of DA 240. He determined a diameter of 10 kpc, derived from high-resolution observations at 5 GHz, implying an effective area of 79 kpc^2. The eastern hot spot of 3C 236 has been observed by Strom & Willis (1980) at 6 cm wavelength. They estimated its angular extent to be $\sim 4''$, corresponding to a linear diameter of 7 kpc. Assuming that the conditions in the other lobe are comparable we obtain an impact area for the 3C 236 jet of 38 kpc^2. For the other sources things are more difficult. Since there are no data available we assume that the extents of hot spots in radio galaxies with similar sizes are of the same order of magnitude. Therefore, we use the mean of the impact areas of DA 240 and 3C 236 as a first guess for the other sources. The effective areas and the resulting densities of the ambient medium have been compiled in Table 6.

Comparing the densities derived in three independent ways we find in all cases a consistent density of the IGM of between $1 \ldots 4 \cdot 10^{-5}$ cm^{-3}. The estimates using ram pressure arguments seem to be the most uncertain since they strongly depend on the jet velocity and the sizes of the impact areas. The advance speed will in general depend on the density profile of the ambient medium, which can be assumed to decrease with increasing
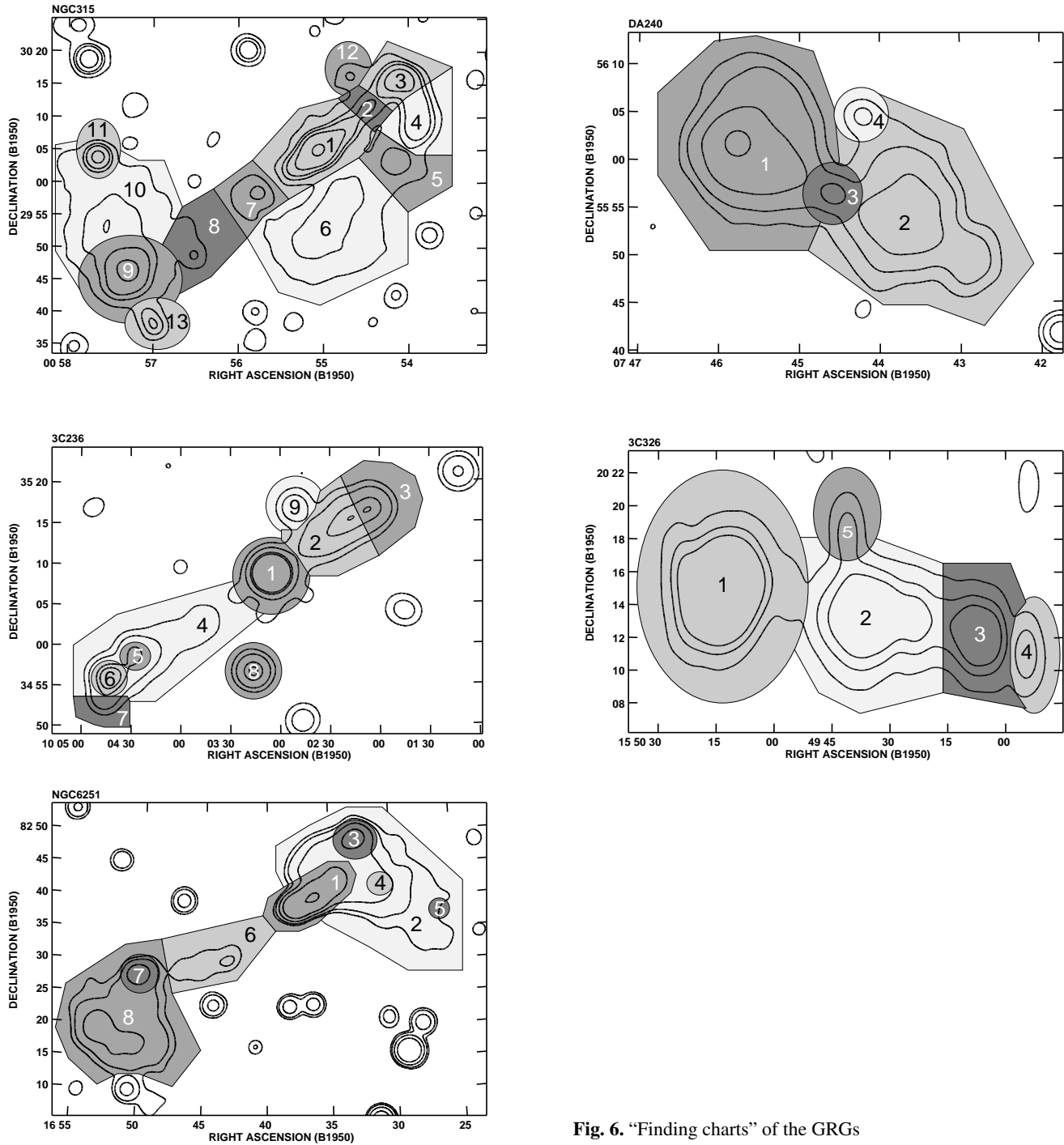
Fig. 6. "Finding charts" of the GRGs

distance from the core. So the advance speed may not be constant, but if we assume that it is a constant value of 0.03c, then the hot spot will move by 0.5 Mpc in $6 \cdot 10^7$ yr. So any synchrotron lifetime which is younger than $6 \cdot 10^7$ yr means that we are seeing fresh particles. So the young ages in Tables 1 – 5 are evidence for reacelleration or resupply of electrons. On the other hand if there is no resupply, it means that the sources advance even faster than 0.03c and the ambient density must be correspondingly lower.

The sizes of the impact areas are also still a matter of discussion. In order to get at least an upper limit for the IGM densities we preferred the identification of the impact areas with the area of a hot spot or a drilling jet at the probable contact zone to the IGM. Therefore, high-resolution observations of these regions would be mandatory to obtain more exact numbers. This would be especially helpful for sources like NGC 315 or NGC 6251. Jet widths closer to the core cannot always be extrapolated to the size of the working area (like in NGC 6251). Sources like

3C 326 without known jets or hot spots form the biggest problem in the determination of intergalactic particle densities as is attempted in this work. A deeper search for indications of the working area in these sources would be valuable.

If we assume the model of Begelman & Cioffi (1989) to be valid also in GRGs our estimate of the IGM density would only be an upper limit. In this case a cocoon of shocked gas which surrounds the radio galaxies would be overpressured compared with the IGM. An upper limit will also be derived if the dentist's drill model (Scheuer 1982) is applied.

In any case, the derived densities are at least one order of magnitude lower than typically found in clusters of galaxies, where GRGs are usually not observed. This implies that the lower density of the ambient medium around the host galaxies of GRGs could be a strong reason for the GRG phenomenon.

5. Summary

We have derived spectral index distributions of the five most extended (in terms of angular size) GRGs. For the first time this was carried out in a frequency range between 326 MHz and 10.6 GHz. This is important since e.g. spectral asymmetries appear to be much more obvious at higher frequencies compared to the appearance at low or intermediate-frequency ranges. The low frequencies are helpful to set constraints to the injection spectral index which is one of the free parameters when fitting synchrotron loss models. The ages resulting from these fits are typical for radio galaxies since they are in the same range as ages found by other authors for smaller-scaled radio galaxies (Alexander & Leahy 1988, Carilli et al. 1991, Klein et al. 1995). This means that particles in GRGs are not any 'older' than, e.g. in smaller-scaled 3C sources. From estimates of the effects of the ambient medium on the sources we obtain particle densities of a few 10^{-5} cm^{-3} which is at least one order of magnitude below the densities derived for smaller-scaled sources, especially those within clusters of galaxies where GRGs are not observed. This argues for the GRGs being so huge because of their low-density environments and not because of higher ages.

References

Alexander P., Leahy J.P., 1987, MNRAS 225, 1
Begelman M.C., Cioffi D.F., 1989, ApJ 345, L21
Bridle A.H., Fomalont E.B., 1978, AJ 83, 704
Burns J.O., Owen F.N., Rudnick L., 1979, AJ 84, 1683
Carilli C., Perley R.A., Dreher J.H., Leahy J.P., 1991, ApJ 283, 554
Daly R.A., 1995, ApJ 454, 580
Fanti R., Lari C., Spencer R.E., Warwick R.S., 1976, MNRAS 174, 5

Jaffe W.J., Perola G.C., 1973, A&A 26, 423
Jägers W.J., 1987, A&AS 71, 75
Kardashev N.S., 1962, Sov. Astron. A. J. 6, 317
Katz-Stone D.M., 1995, Ph.D. thesis, University of Minnesota
Klein U., Mack K.-H., Gregorini L., Parma P., 1995, A&A 303, 427
Klein U., Mack K.-H., Saripalli L., 1996, Proceedings IAU Symp. 175, ed. Ekers R., Fanti C., Padrielli L., Kluwer Academic Publishers, p. 311
Lacy M., Rawlings S., Saunders R., Warner P.J., 1993, MNRAS 264, 721
Mack K.-H., Klein U., O'Dea C.P., Willis A.G., 1997, A&AS 123, 463
Myers S.T., Spangler S.R., 1985, ApJ 291, 52
Nath B.B., 1995, MNRAS 274, 208
O'Dea C.P., Baum S.A., 1997, ApJ 113, 148
Pacholczyk A.G., 1970, Radio Astrophysics, Freeman, San Francisco
Perley R.A., Bridle A.H., Willis A.G., 1984, ApJS 54, 291
Roland J., Hanisch R.J., Pelletier G., 1990, A&A 231, 327
Roland J., Hanisch R.J., Veron P., Fomalont E., 1985, A&A 148, 323
Roland J., Rhee G.F.R.N., 1989, A&A 213, 10
Rudnick L., Katz-Stone D.M., 1996, in: Energy Transport in Radio Galaxies and Quasars, Hardee P.E., Bridle A.H., Zensus J.A. (eds.) ASP Conf. Ser. 100
Saunders R., Baldwin J.E., Pooley G.G., Warner P.J., 1981, MNRAS 197, 287
Saripalli L., 1988, Ph.D. thesis, Indian Institute of Science, Bangalore
Scheuer P.A.G., 1982, in Heeschen D.S., Wade C.M., eds. Proc. IAU Symp. 97, Extragalactic Radio Sources, Reidel, Dordrecht, p. 163
Scheuer P.A.G., 1995, MNRAS 277, 331
Strom R.G., Baker J.R., Willis A.G., 1981, A&A 100, 220
Strom R.G., Willis A.G., 1980, A&A 85, 36
Subrahmanyan R., Saripalli L., 1993, MNRAS 260, 908
Tsien S.C., 1982, MNRAS 200, 377
van der Laan H., Perola G.C., 1969, A&A 3, 468
Waggett P.C., Warner P.J., Baldwin J.E., 1977, MNRAS 181, 465
Willis A.G., Strom R.G., 1978, A&A 62, 375
Willis A.G., Strom R.G., Bridle A.H., Fomalont E.B., 1981, A&A 95, 250